body in sharks and a regionalized body with a pivoting neck joint and rigid trunk armor in arthrodires. Their evolutionary importance hinges on whether eubrachythoracid musculature is specialized or primitive relative to that of sharks. Placoderms appear to be a paraphyletic segment of the gnathostome stem group (*3*, *4*), so if any components of eubrachythoracid musculature can be shown to be general for placoderms, they can also be inferred to be primitive relative to the crown group. The status of the shallow myoseptal curvature cannot yet be determined in this regard, but the muscles of the neck joint and abdomen have specific skeletal associations that allow such phylogenetic inferences to be drawn.

Most ostracoderms, a grade of jawless stem gnathostomes (*2*) (Fig. 1A), have head shields that also encompass the shoulder-girdle region (*2*). This suggests that the gnathostome shoulder girdle originated through subdivision of the shield. Almost all placoderms have a mobile joint between the skull and shoulder girdle, implying the need for elevator and depressor muscles such as those observed in eubrachythoracids. Thus, a cucullaris operating this joint, antagonistic to specialized epaxial head elevators, is probably primitive relative to the crown gnathostome condition of a cucullaris without specialized antagonists that forms part of a broadly flexible neck.

The transverse abdominal muscles of eubrachythoracids are not as directly tied to a skeletal structure with an identifiable mechanical function. Comparison with those of a recent elephant shark indicates that these muscles are not homologous with any muscles of the pelvic fin or male clasper (supplementary text). However, the transverse abdominals may modulate shear forces between the armor and the laterally undulating body during tail-propelled swimming. A long ventral armor is also present in antiarchs, recovered as the most primitive placoderms in several recent analyses (*3*, *4*, *15*). Transverse abdominal muscles may thus be an attribute of the placoderm segment of the gnathostome stem group and, hence, primitive relative to the absence of such muscles at the base of the gnathostome crown group.

Outside of placoderms, transversely oriented abdominal muscle fibers are restricted to tetrapods and have been regarded as a tetrapod autapomorphy (*16*). Their associated connective tissues and tendons are derived from the somatopleure component of the lateral plate mesoderm (*17*), which plays an important role in hypaxial myogenesis (*18*). In lampreys, the posterior lateral plate mesoderm is not separated into splanchnic and somatopleuric components (*19*), meaning that it cannot give rise to somatopleure-derived structures such as paired fins. The presence of paired fins in placoderms shows that separation of somatopleure and splanchnopleure had occurred, supporting the inference that their transverse muscles may have been patterned by the same somatopleure-based mechanism as in tetrapods.

The arthodires of the Gogo Formation reveal an elaborate regionalized musculature, including the earliest and phylogenetically deepest examples of several muscle types. Particularly surprising is the extensive development of transverse-fiber muscles in the ventral body wall, which parallels the condition in tetrapods. Hypothetical reconstructions are not able to recover the full complexity of this musculature, either on the basis of biomechanical analysis or phylogenetic bracketing, and are thus liable to give a false picture of muscular evolution at the origin of gnathostomes. The study of exceptionally preserved fossils will continue to provide essential data for the reconstruction of vertebrate soft anatomy, particularly in groups with no close living relatives.

References and Notes

1. Y. Oisi, K. G. Ota, S. Kuraku, S. Fujimoto, S. Kuratani, *Nature* **493**, 175–180 (2013).
2. P. Janvier, *Early Vertebrates* (Clarendon Press, Oxford, 1996).
3. M. D. Brazeau, *Nature* **457**, 305–308 (2009).
4. S. P. Davis, J. A. Finarelli, M. I. Coates, *Nature* **486**, 247–250 (2012).
5. T. Matsuoka *et al.*, *Nature* **436**, 347–355 (2005).
6. J. Mallatt, *Zool. J. Linn. Soc.* **117**, 329–404 (1996).
7. S. Kuratani, *J. Anat.* **205**, 335–347 (2004).
8. S. Kuratani, *Dev. Growth Differ.* **50** (suppl. 1), S189–S194 (2008).
9. A. Heintz, in *The Bashford Dean Memorial Volume: Archaic Fishes*, E. W. Gudger, Ed. (American Museum of Natural History, New York, 1930), pp. 115–224.
10. R. Miles, T. S. Westoll, *Trans. R. Soc. Edinb.* **67**, 373–476 (1968).
11. F. H. Edgeworth, *The Cranial Muscles of Vertebrates* (Cambridge Univ. Press, Cambridge, 1935).
12. K. Trinajstic, C. Marshall, J. Long, K. Bifield, *Biol. Lett.* **3**, 197–200 (2007).
13. S. Gemballa *et al.*, *Proc. Biol. Sci.* **270**, 1229–1235 (2003).
14. S. A. Wainwright, F. Vosburgh, J. H. Hebrank, *Science* **202**, 747–749 (1978).
15. M. Zhu, X. Yu, B. Choo, J. Wang, L. Jia, *Biol. Lett.* **8**, 453–456 (2012).
16. N. Schilling, *Front. Zool.* **8**, 4 (2011).
17. B. Christ, M. Jacob, H. J. Jacob, *Anat. Embryol.* **166**, 87–101 (1983).
18. S. J. Mathew *et al.*, *Development* **138**, 371–384 (2011).
19. K. Onimaru, E. Shoguchi, S. Kuratani, M. Tanaka, *Dev. Biol.* **359**, 124–136 (2011).

Acknowledgments: We acknowledge M. Siversson at the Western Australian Museum, Perth, and Z. Johanson at the Natural History Museum, London, for lending us specimens in their care. We thank I. Montero Verdú for his picture of the muscle bundles (Fig. 3D) and A. Ritchie for an *Eastmanosteus* image. K.T., P.E.A., and C.B. are supported by Australian Research Council (ARC) QEII Fellowship DP 110101127; J.L., K.T., T.S., and G.Y. by ARC DP 1092870; S.S., V.D., and P.E.A. by European Research Council Advanced Investigator Grant 233111; P.E.A. by a Wallenberg Scholarship from the Knut and Alice Wallenberg Foundation; and C.B. by a Human Frontiers Research Program and an ARC Discovery Project, DP 1096002. The scan performed at the European Synchrotron Radiation Facility in Grenoble, France, was part of project EC770. K.T. acknowledges the 2010 Prime Minister's Science Prize, and J.L. acknowledges funding from The Australian Geographic Society, which supported fieldwork at the Gogo Formation. Specimens are housed in the collections of the Western Australian Museum, Australian National University, Australian Museum, and Museum Victoria, Australia, and the Natural History Museum, UK.

Supplementary Materials

www.sciencemag.org/cgi/content/full/science.1237275/DC1
Materials and Methods
Supplementary Text
Figs. S1 to S4
References (*20*–*30*)
Movie S1

4 March 2013; accepted 29 May 2013
Published online 13 June 2013;
10.1126/science.1237275

Enhanced Remote Earthquake Triggering at Fluid-Injection Sites in the Midwestern United States

Nicholas J. van der Elst,[1]* Heather M. Savage,[1] Katie M. Keranen,[2]† Geoffrey A. Abers[1]

A recent dramatic increase in seismicity in the midwestern United States may be related to increases in deep wastewater injection. Here, we demonstrate that areas with suspected anthropogenic earthquakes are also more susceptible to earthquake-triggering from natural transient stresses generated by the seismic waves of large remote earthquakes. Enhanced triggering susceptibility suggests the presence of critically loaded faults and potentially high fluid pressures. Sensitivity to remote triggering is most clearly seen in sites with a long delay between the start of injection and the onset of seismicity and in regions that went on to host moderate magnitude earthquakes within 6 to 20 months. Triggering in induced seismic zones could therefore be an indicator that fluid injection has brought the fault system to a critical state.

Earthquakes can be induced by underground fluid injection, which increases pore pressure and allows faults to slide under preexisting shear stress (*1*). The increase in wastewater disposal from natural gas development and other sources has been accompanied by an increase in fluid-induced earthquakes in recent years (*2*). These earthquakes include widely felt earthquakes in

The musculature of eubrachythoracid arthrodires, characterized by shallow myoseptal curvature, differentiated head elevators positioned as antagonists to the cucullaris, and bands of transverse-fiber muscles in the abdomen, differs greatly from that of sharks. The latter is dominated by deeply W-shaped myomeres, lacks transverse abdominal muscles, and includes a broadly flexible neck region with a narrow triangular cucullaris forming a dorsal edge to the branchial chamber (*11*, *13*). Most of the differences appear to reflect the overall contrast between a relatively uniform, flexible

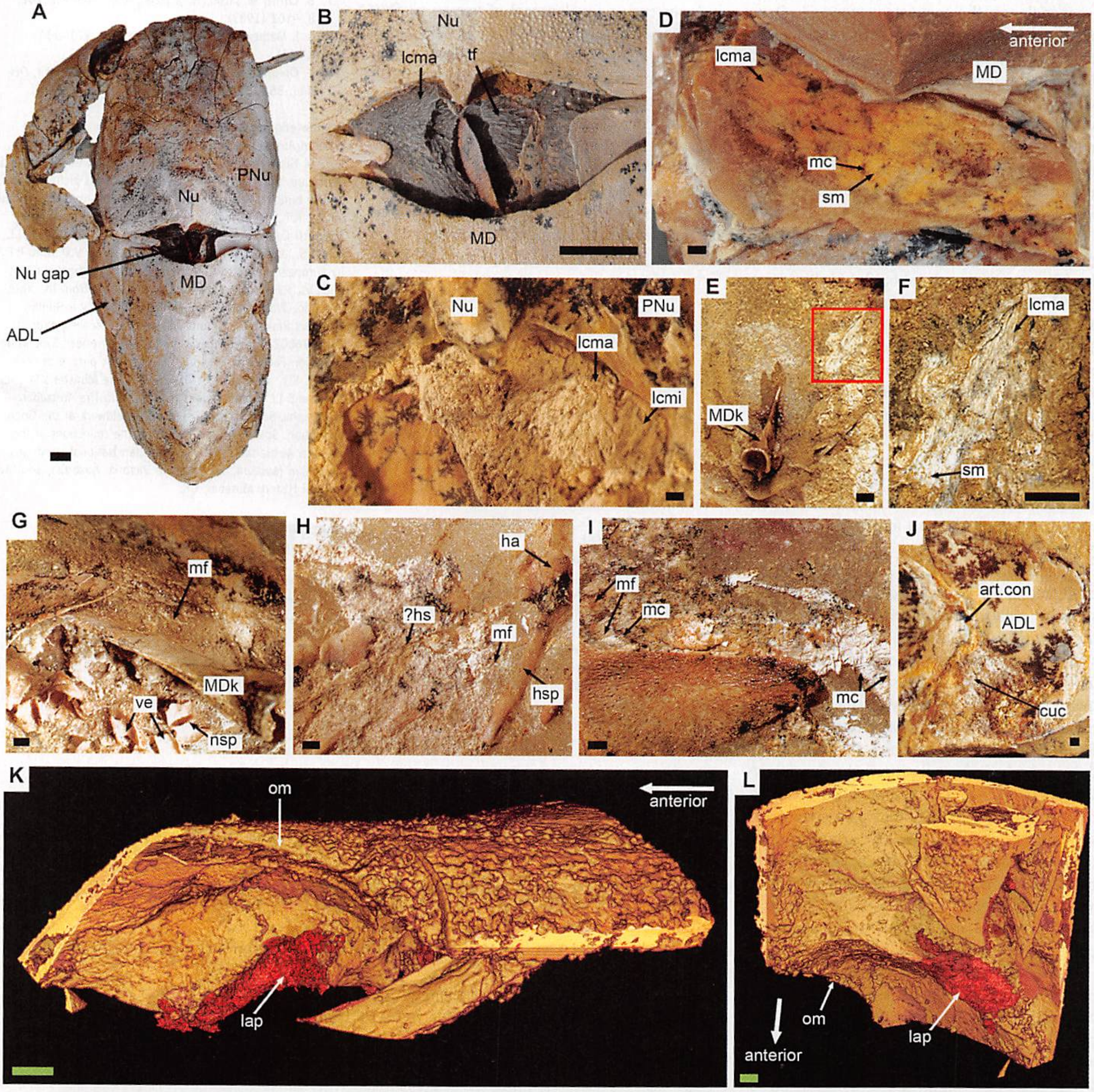

Fig. 3. Muscle preservation. (**A**) *Eastmanosteus* [Australian National University (ANU) specimen V2582] in dorsal view showing the nuchal gap. (**B**) Detailed view of ANU V2582. (**C**) *Compagopiscis* (WAM 11.12.05) in dorsal view, showing the levator capitis major and minor. (**D**) Dorsolateral view of *Incisoscutum* (WAM 10.01.02) levator capitis major and segmented trunk muscles underlying the median dorsal plate. (**E** and **F**) *Incisoscutum* (WAM 95.1.1); internal view of median dorsal plate with muscle fibers. (F) Magnification of red box in (E). (**G** to **I**) *Incisoscutum* (NHM P50934). (G) Vertebral elements below the median dorsal plate. (H) Proposed horizontal myoseptum. (I) Trunk muscles. (**J**) Cucullaris muscle of *Compagopiscis* (WAM 11.12.05), attached to the internal surface of the anterior dorsolateral plate. (**K** and **L**) *Compagopiscis* (WAM 12.8.1), showing levator arcus palatini attaching to the left ventral postocular process. (K) Lateral view; (L) posteroventral view. Scale bars: (A) and (B), 10 mm; (C) to (L), 1 mm. Abbreviations are as in Fig. 2, plus: art. con, articular condyle of neck joint; cuc, cucullaris; ?hs, possible horizontal septum; ha, hemal arch; hsp, hemal spine; lap, levator arcus palatini; lcma, levator capitis major; lcmi, levator capitis minor; mc, myocomma; MDk, median dorsal keel; mf, muscle fibers; Nu gap, nuchal gap; om, orbital margin; sm, segmented muscle block; ve, vertebral elements.

Oklahoma, Arkansas, Ohio, Texas, and Colorado (Fig. 1) (*3*–*7*). Although most injection wells are not associated with large earthquakes, the converse is not true. At least half of the 4.5 moment magnitude (M_w) or larger earthquakes to strike the interior of the United States in the past decade have occurred in regions of potential injection-induced seismicity (table S1). In some cases, the onset of seismicity follows injection by only days or weeks (*1*, *3*, *5*), and the association with pumping at particular wells is clear. In others, seismicity increases only after months or years of active injection (*4*, *8*, *9*).

A long delay before seismic activation implies that faults may be moving toward a critical state for years before failure. However, currently there are no reliable methods to determine whether a particular field has reached a critical state other than by simply observing a large increase in seismicity. This lack of diagnostics is a key problem in developing operational strategies to mitigate anthropogenic activity (*2*).

Because induced seismic zones are brought to failure by increased pore pressures, we examined whether areas of induced seismicity show a high susceptibility to dynamic triggering by the small transient stresses carried by seismic waves from distant earthquakes. Dynamic triggering in natural settings has been linked to the presence of subsurface fluids, and seismicity rate changes have been shown to depend systematically on the perturbation stress (*10*–*13*). This suggests that dynamic triggering could serve as a probe of the state of stress in areas of wastewater injection. We refer to earthquakes that are promoted by anthropogenic activity as induced and to earthquakes that are initiated by transient natural stresses as triggered. By this definition, there can be triggered induced earthquakes.

A search of the Advanced National Seismic System (ANSS) earthquake catalog gives preliminary evidence that induced seismic zones are sensitive to dynamic triggering by surface waves (Fig. 1). Regions of suspected induced seismicity showed a pronounced increase in 3.0 *M* and larger earthquakes spanning at least a 3-day window after large ($M_\mathrm{w} \geq 8.6$) remote earthquakes: the 27 February 2010 8.8 M_w Maule, Chile; 11 March 2011 9.1 M_w Tohoku-oki; and 12 April 2012 8.6 M_w Sumatra earthquakes. The broader central United States shows essentially no response to these events (Fig. 1). Most of the triggering is at three sites: Prague, Oklahoma; Snyder, Texas; and Trinidad, Colorado. Suggestively, each of these regions went on to host moderate to large earthquakes (4.3 to 5.7 M_w) within 6 to 20 months of the strong triggering.

Although the triggering is significant at the 96% level (table S2), a closer investigation is warranted. We therefore enhanced the catalog by applying a single-station matched filter to continuous waveforms (*14*). The matched-filter approach identifies small, uncataloged earthquakes based on their similarity to target events (*15*–*17*). Distinct families of earthquakes are distinguished based on the difference in *P* and *S* wave travel times (*S-P* time), which gives the approximate radial distance from the seismic station (*15*).

The Cogdell oil field (*8*), located near Snyder, Texas, hosted a seismic swarm in September 2011 that included a 4.3 M_w main shock (supplementary text). The enhanced catalog shows that the Tohoku-oki earthquake triggered a significant number of earthquakes (*14*) at this site (Fig. 2 and table S2). In fact, the rate of earthquakes within the 10 days after the Tohoku-oki earthquake was the highest observed over the entire study duration (February 2009 to present), excluding the days immediately after the 4.3 M_w main shock. The triggered earthquakes show a swarm like signature, typical of fluid-induced earthquakes (*18*), with the largest of the triggered events (3.8 M_w, ANSS) occurring after 2.5 days of smaller events (Fig. 2C). The much earlier February 2010 Maule earthquake did not trigger at Snyder, nor did the post-swarm April 2012 Sumatra earthquake.

Prague, Oklahoma, experienced three 5.0 M_w and greater earthquakes in November 2011, associated with fluid disposal in the Wilzetta field (supplementary text) (*4*). The enhanced catalog shows that the February 2010 Maule event triggered a strong sequence of earthquakes near the eventual epicenter of the first 5.0 M_w earthquake (Fig. 3 and table S2). The rate of earthquakes in the several days after the Maule trigger far exceeds that of any other time within the period of observation, up to the $M_\mathrm{w} \geq 5.0$ earthquakes themselves, which is similar to the observation at Snyder. There are no events detected within ±32 km relative distance for at least 4 months before the 2010 Maule earthquake.

The largest event in the remotely triggered sequence is a 4.1 M_w, 16 hours after the 2010 Maule earthquake, which may account for the large number of earthquakes that continued up to the time of the first 5 M_w Prague earthquake in 2011 (Fig. 3). If the 4.1 M_w earthquake can be considered a foreshock of the subsequent 5.7 M_w Prague earthquake, then the 5.7 M_w event is not only one of the largest earthquakes to be associated with wastewater disposal (*2*) but also one of the largest earthquakes to be linked indirectly to a remote triggering event (*4*, *19*).

The April 2011 Tohoku-oki earthquake, which occurred during the ongoing sequence before the 5.7 M_w Prague main shock, did not trigger additional earthquakes near the swarm (Fig. 3 and table S2). The 2012 Sumatra earthquake, on the other hand, followed the main 5.7 M_w Prague earthquake by 5 months and triggered a small uptick in activity that was consistent with the far northeastern tip of the swarm (Fig. 3C). However, this triggered rate change is much smaller than that triggered by the Maule earthquake in 2010.

Trinidad, Colorado, experienced a seismic swarm in August 2011 that included a 5.3 M_w main shock, possibly related to coal-bed methane extraction and reinjection of the produced water in the Raton Basin (supplementary text). The February 2010 Maule earthquake triggered a small but statistically significant response near the site of the 5.3 M_w main shock (Fig. 4 and table S2). Although the total number of triggered events is small (four), the binomial probability of observ-

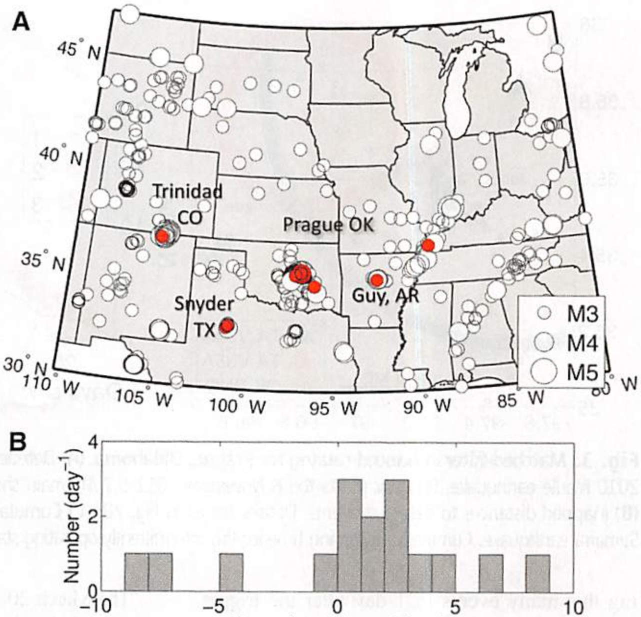

Fig. 1. Remote triggering in the midwestern United States, from the composite ANSS catalog. (A) Cataloged earthquakes above 3.0 *M* between 2003 and 2013 (ANSS). Earthquakes in red occurred during the first 10 days after the February 2010, Maule; March 2011, Tohoku-oki; or April 2012, Sumatra earthquakes. Triggering occurs almost exclusively in three injection fields, labeled Prague, Trinidad, and Snyder. **(B)** Stacked earthquake counts in the 10 days before and after the three ≥8.6 M_w remote earthquakes. The histogram excludes the Guy, Arkansas, swarm, which dominates event rates at the time of the 2011 Tohoku-oki earthquake but did not trigger (supplementary text).

[1] Lamont-Doherty Earth Observatory of Columbia University, Post Office Box 1000, 61 Route 9W, Palisades, NY 10964, USA. [2] ConocoPhillips School of Geology and Geophysics, University of Oklahoma, 100 East Boyd Street, Norman, OK 73069, USA.
*Corresponding author. E-mail: nicholas@ldeo.columbia.edu
†Present address: Department of Earth and Atmospheric Sciences, Cornell University, 410 Thurston Avenue, Ithaca, NY 14850, USA.

Fig. 2. Matched-filter enhanced catalog for Snyder, Texas. (**A**) Detected events, showing triggering by the 2011 Tohoku-oki earthquake. Symbols along top show strength of triggering (red, strong; green, none). Red star marks 11 September 2011 4.3 M_w main shock (NEIC catalog). Colors correspond to station in (B), with ANSS catalog in gray. Seismometer operating times and the times at which we have enhanced the catalog are shown by thin and thick horizontal bars, respectively. (**B**) Mapped distances to detected events. Small circles are ANSS catalog earthquakes; a red star shows the main shock. Yellow squares are nearby active injection wells. (**C**) Cumulative event count around the 2010 Maule and 2011 Tohoku-oki earthquakes.

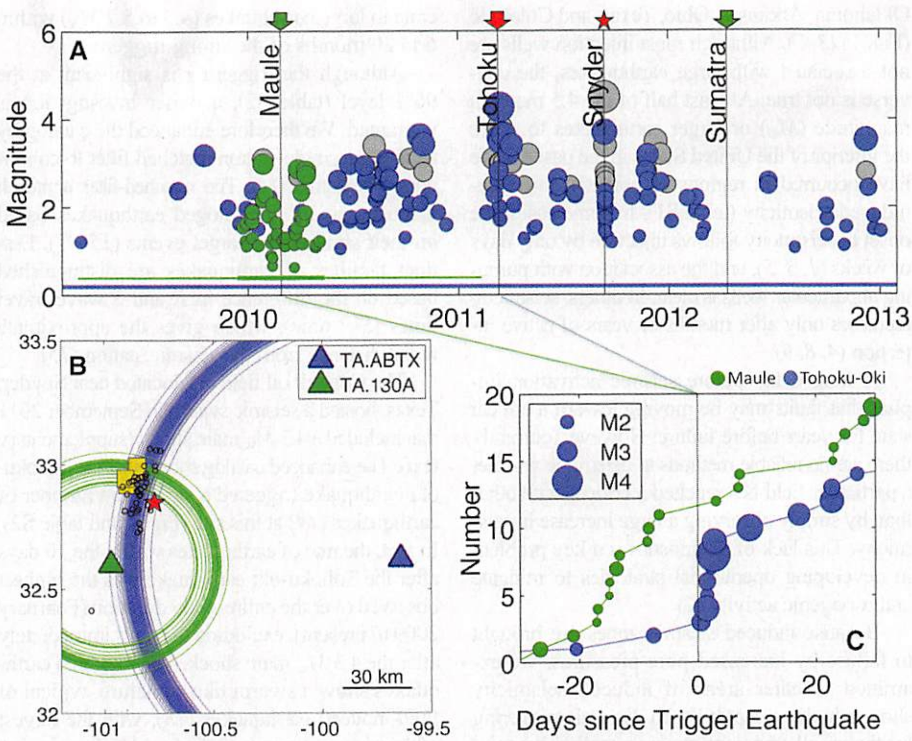

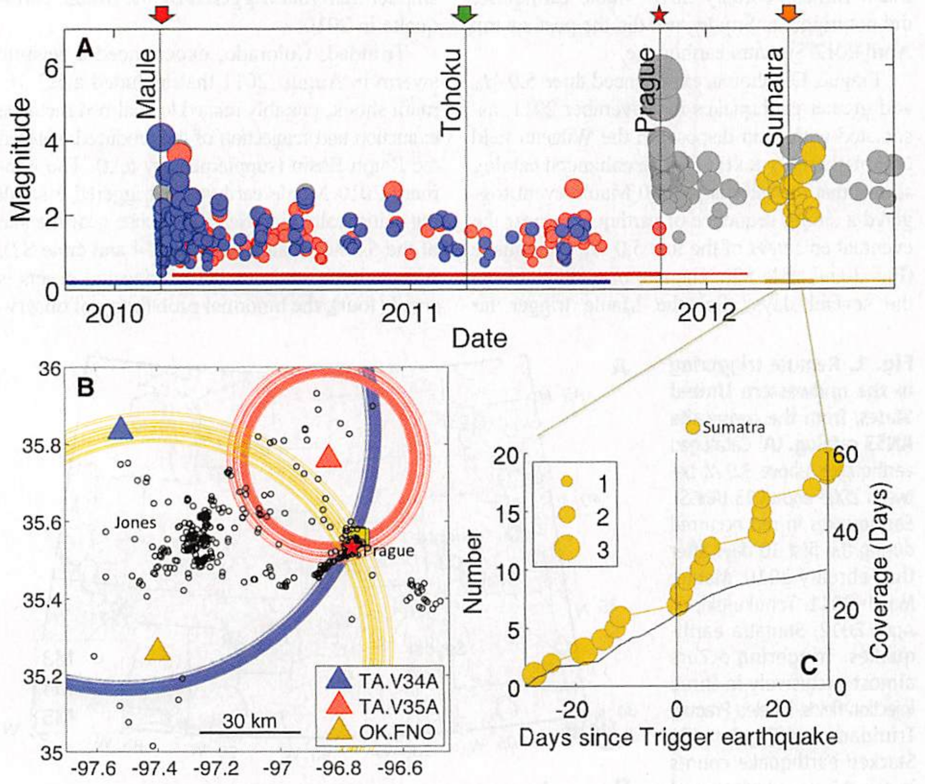

Fig. 3. Matched-filter enhanced catalog for Prague, Oklahoma. (**A**) Detected events, showing triggering by the 2010 Maule earthquake. Red star marks the 6 November 2011 5.7 M_w main shock. Other details are as in Fig. 2A. (**B**) Mapped distances to detected events. Details are as in Fig. 2B. (**C**) Cumulative event count around the 2012 Sumatra earthquake. Cumulative recording time for this intermittently operating station is shown over the same period.

ing this many events in 1 day after the trigger, given five events in the entire previous year, is less than 10^{-5}.

The March 2011 Tohoku-oki earthquake, which occurred during the active portion of the swarm, did not trigger additional seismicity at Trinidad. The 2012 Sumatra earthquake occurred 8 months after the 5.3 M_w Trinidad main shock and triggered a moderate surge in activity that was consistent with the far edge of the swarm, where previous swarm activity had not occurred (fig. S2). This pattern—strong triggering by the first remote earthquake, none by the second, and marginal triggering after the swarm—is very similar to that observed in Oklahoma.

We examined several other regions in the United States that have experienced moderate magnitude earthquakes or heightened seismicity rates linked to fluid injection, including Guy, Arkansas; Jones, Oklahoma; and Youngstown, Ohio. None of these other regions appear to have responded to remote triggering (supplementary text).

The strongly triggered regions were exceptional in that they had a long history of pumping within 10 km of the eventual swarms yet were relatively quiet for much of that history. At other sites of induced moderate earthquakes (Guy, Arkansas, and Youngstown, Ohio), the lag time between the start of pumping and onset of seismicity was as little as months or weeks, presenting a relatively small window of vulnerability to dynamic triggering before the swarms.

The delay in induced seismicity in some regions could be due to complexities in the local geology (supplementary text). In Oklahoma, injection occurred into a fault-bounded pocket, and pressures may have built up slowly over time because of the size of the reservoir bounded by impermeable faults (*4*). The Cogdell field may have similar isolated pockets, formed by discrete carbonate reefs buried within impermeable shales (*8*).

Fluids have been suggested as an important component in dynamic triggering since early

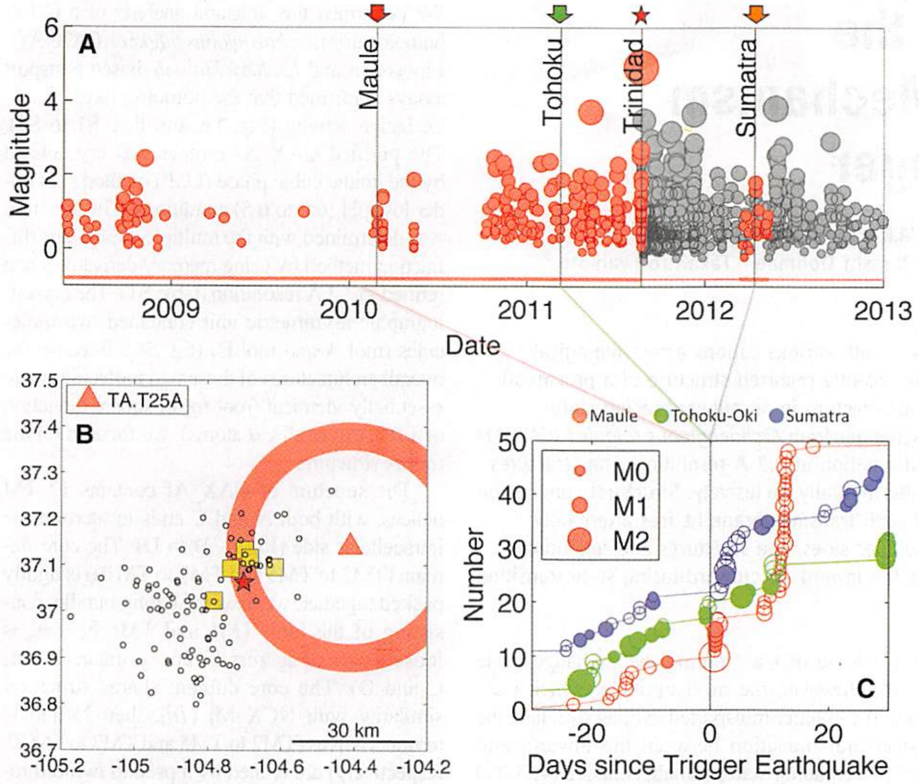

Fig. 4. Matched-filter enhanced catalog for Trinidad, Colorado. (**A**) Detected events, showing triggering by the 2010 Maule earthquake. Red star marks the 23 August 2011 5.3 M_w main shock. Other details are as in Fig. 2A. (**B**) Mapped distances to detected events. Details are as in Fig. 2B. (**C**) Waveform detection counts around the 2010 Maule, 2011 Tohoku-oki, and 2012 Sumatra earthquakes (curves offset for clarity). Filled circles are within 2.5-km radial distance relative to the 5.3 M_w main shock, and open circles are within ~5 km (fig. S2).

observations showed preferential triggering in active volcanic and hydrothermal systems (*13*, *20*, *21*). Some features of our observations are also suggestive of a fluid mechanism for triggering. First, in all of the studied cases the triggered earthquakes occurred with a small delay with respect to the passage of the seismic waves, initiating within less than 24 hours and continuing for days to months afterward. This pattern suggests a triggering mechanism that relies on dynamic permeability enhancement and transport of fluids (*22*, *23*), as has been suggested for natural triggered seismicity (*20*–*22*). In this scenario, stress transients alter the permeability of hydraulic conduits in the reservoir, accelerating diffusion of pore pressure into local faults. Fractures in active injection reservoirs may be particularly susceptible to this mechanism because the injection of unequilibrated fluids may lead to clogging through mineralization and sedimentation. A brief pressure transient may then flush out these clogged fractures (*22*, *24*).

In Prague and Trinidad, only the first of two large remote events caused earthquakes, despite imparting dilational and shear strains that are similar to subsequent events (table S4). This is also consistent with the permeability enhancement model, which requires a certain amount of recharge time between triggering episodes (*24*). After local fault slip is triggered, the local permeability rises dramatically because of microfracturing and dilation (*25*), promoting further fluid diffusion over several rupture dimensions (*26*). Hence, once the seismic swarm is underway the fractures may not return to a state in which they are susceptible to unclogging by small transient stresses.

We find that certain areas of fluid injection are sensitive to small changes in stress associated with the passage of seismic waves from remote large earthquakes. The observations suggest several requirements for an induced region to be sensitive to remote triggering. First, all of the triggered sites in this study had a long history of regional subsurface injection over a period of decades. Second, each triggered site was near to hosting a moderate magnitude earthquake, suggesting critically stressed faults. Last, each site had relatively low levels of seismicity rate in the immediate vicinity (10 km) before the first triggering episode. Remote triggering can therefore indicate that conditions within an injection field have crossed some critical threshold, and a larger induced earthquake could be possible or even likely. This underlines the importance of improved seismic monitoring in areas of subsurface fluid injection.

References and Notes

1. C. B. Raleigh, J. H. Healy, J. D. Bredehoeft, *Science* **191**, 1230–1237 (1976).
2. National Research Council, *Induced Seismicity Potential in Energy Technologies* (National Academies Press, New York, 2012).
3. S. Horton, *Seismol. Res. Lett.* **83**, 250–260 (2012).
4. K. M. Keranen, H. M. Savage, G. A. Abers, E. S. Cochran, *Geology* **41**, 699–702 (2013).
5. W.-Y. Kim, "Induced seismicity associated with fluid injection into deep wells in Youngstown, Ohio," abstract S43D-2496 presented at 2012 Fall Meeting, American Geophysical Union, San Francisco, CA, 3 to 7 December 2012.
6. C. Frohlich, J. Glidewell, M. Brunt, *Bull. Seismol. Soc. Am.* **102**, 457–466 (2012).
7. J. L. Rubinstein, W. L. Ellsworth, A. McGarr, "The 2001–present triggered seismicity sequence in the Raton basin of southern Colorado/Northern New Mexico," BSSA Abstracts 2013 Annual Meeting 155D, (2013).
8. S. D. Davis, W. D. Pennington, *Bull. Seismol. Soc. Am.* **79**, 1477–1494 (1989).
9. R. B. Horner, J. E. Barclay, J. M. MacRae, *Can. J. Explor. Geophys.* **30**, 39–50 (1994).
10. N. J. van der Elst, E. E. Brodsky, *J. Geophys. Res.* **115**, B07311 (2010).
11. H. M. Savage, C. Marone, *J. Geophys. Res.* **113**, B05302 (2008).
12. D. P. Hill, S. G. Prejean, in *Dynamic Triggering*, vol. 4, H. Kanamori, Ed., Treatise on (Elsevier, New York, 2007), pp. 257 to 292.
13. D. P. Hill *et al.*, *Science* **260**, 1617–1623 (1993).
14. Materials and methods are available as supplementary materials on *Science* Online.
15. C. Frohlich, C. Hayward, B. Stump, E. Potter, *Bull. Seismol. Soc. Am.* **101**, 327–340 (2011).
16. Z. G. Peng, P. Zhao, *Nat. Geosci.* **2**, 877–881 (2009).
17. D. R. Shelly, G. C. Beroza, S. Ide, *Nature* **446**, 305–307 (2007).
18. J. E. Vidale, P. M. Shearer, *J. Geophys. Res.* **111**, B05312 (2006).
19. T. Parsons, A. A. Velasco, *Nat. Geosci.* **4**, 312–316 (2011).
20. E. E. Brodsky, S. G. Prejean, *J. Geophys. Res.* **110**, B04302 (2005).
21. S. Husen, R. Taylor, R. B. Smith, H. Healser, *Geology* **32**, 537–540 (2004).
22. E. E. Brodsky, E. Roeloffs, D. Woodcock, I. Gall, M. Manga, *J. Geophys. Res.* **108**, (B8), 2390 (2003).
23. T. Taira, P. G. Silver, F. L. Niu, R. M. Nadeau, *Nature* **461**, 636–639 (2009).
24. J. E. Elkhoury, A. Niemeijer, E. E. Brodsky, C. Marone, *J. Geophys. Res.* **116**, (B2), B02311 (2011).
25. T. M. Mitchell, D. R. Faulkner, *J. Geophys. Res.* **113**, (B11), B11412 (2008).
26. S. Micklethwaite, S. F. Cox, *Earth Planet. Sci. Lett.* **250**, 318–330 (2006).

Acknowledgments: This paper benefitted from discussions with E. Brodsky and W.-Y. Kim. Injection data for Cogdell Oilfield was provided by C. Frohlich. The Oklahoma Corporation Commission, the Texas Railroad Commission, and the Colorado Oil and Gas Conservation Commission supplied well databases. Earthquake locations were provided by ANSS. Seismic waveforms are from the Incorporated Research Institutions for Seismology Data Management Center. N.J.v.d.E. was supported by U.S. National Science Foundation (NSF) grant EAR-1144503. H.M.S. and G.A.A. were partially supported by U.S. Geological Survey (USGS) National Earthquake Hazards Reduction Program (NEHRP) grant G13AP00024. K.M.K. received support from USGS NEHRP grant G13AP00025. This project made use of EarthScope's Transportable Array, a facility funded by NSF. The enhanced seismicity catalogs are available as supplementary materials on *Science* Online.

Supplementary Materials

www.sciencemag.org/cgi/content/full/341/6142/164/DC1
Materials and Methods
Supplementary Text
Figs. S1 to S5
Tables S1 to S5
References (*27*–*43*)
Database S1

9 April 2013; accepted 23 May 2013
10.1126/science.1238948

Structural Basis for the Counter-Transport Mechanism of a H^+/Ca^{2+} Exchanger

Tomohiro Nishizawa,[1,2] Satomi Kita,[3] Andrés D. Maturana,[4] Noritaka Furuya,[1] Kunio Hirata,[5] Go Kasuya,[1] Satoshi Ogasawara,[6] Naoshi Dohmae,[2] Takahiro Iwamoto,[3] Ryuichiro Ishitani,[1,2]* Osamu Nureki[1,2]*

Ca^{2+}/cation antiporters catalyze the exchange of Ca^{2+} with various cations across biological membranes to regulate cytosolic calcium levels. The recently reported structure of a prokaryotic Na^+/Ca^{2+} exchanger (NCX_Mj) revealed its overall architecture in an outward-facing state. Here, we report the crystal structure of a H^+/Ca^{2+} exchanger from *Archaeoglobus fulgidus* (CAX_Af) in the two representatives of the inward-facing conformation at 2.3 Å resolution. The structures suggested Ca^{2+} or H^+ binds to the cation-binding site mutually exclusively. Structural comparison of CAX_Af with NCX_Mj revealed that the first and sixth transmembrane helices alternately create hydrophilic cavities on the intra- and extracellular sides. The structures and functional analyses provide insight into the mechanism of how the inward- to outward-facing state transition is triggered by the Ca^{2+} and H^+ binding.

Calcium ions are involved in diverse physiological processes, such as muscle contraction, cell proliferation, exocytosis, and apoptosis (*1*–*3*). The Ca^{2+}/cation antiporter (CaCA) superfamily members are important regulators of cytosolic Ca^{2+} levels (*4*–*6*). They use the electrochemical gradient of other cations—such as Na^+, H^+, or K^+—to catalyze Ca^{2+} transport across biological membranes (*4*–*6*). The CaCA superfamily comprises five major groups: Na^+/Ca^{2+} exchangers (NCX), K^+-dependent Na^+/Ca^{2+} exchangers (NCKX), H^+/Ca^{2+} exchangers (CAX), cation/Ca^{2+} (other cation than Na^+, H^+, or K^+) exchangers (CCX), and the bacterial homologous gene (*YrbG*) (*6*, *7*). All CaCA proteins contain two highly conserved α-repeat regions (α-1 and α-2), which are thought to have arisen from an ancient gene duplication event (*6*, *8*) and are reportedly important for cation binding and transport (*8*–*10*).

Recently, the crystal structure of the Na^+/Ca^{2+} exchanger from *Methanococcus jannaschii* (NCX_Mj) in an outward-facing state was reported, revealing a pseudosymmetric architecture formed by two structural repeats of five transmembrane (TM) helices with opposite orientations (*10*). Three Na^+ sites and one Ca^{2+}-specific site were observed within the cation binding pocket, leading to an exchange model in which the sequential binding of three Na^+ ions causes the release of Ca^{2+} during the exchange cycle (*10*). However, the mechanism by which Ca^{2+} and the counter-transported cations stimulate the structural transition between the inward- and outward-facing states remains elusive (*4*, *5*, *11*) because of the lack of the structural information of its inward-facing state. Furthermore, the molecular basis for the cation recognition in other members of the CaCA superfamily remains unclear.

We performed the structural analysis of a CaCA homolog from *Archaeoglobus fulgidus* (CAX_Af). Liposome- and *Escherichia coli*–based transport assays confirmed that the homolog has H^+/Ca^{2+} exchange activity (Fig. 1A and figs. S1 to S3). The purified CAX_Af protein was crystallized by the lipidic cubic phase (LCP) method (*12*) under low-pH (6.0 to 6.5) conditions. The structure was determined with the multiple anomalous diffraction method by using mercury derivatives and refined to 2.3 Å resolution (table S1). The crystallographic asymmetric unit contained two molecules (mol A and mol B) (fig. S4). Because the overall architectures of these two molecules were essentially identical (root mean square deviation of 1.04 Å over all Cα atoms), we focused on the mol A structure.

The structure of CAX_Af contains 12 TM helices, with both N and C ends located on the intracellular side (Fig. 1, B to D). The core domain (TM2 to TM5 and TM7 to TM10) is tightly packed together, whereas the gating bundle, consisting of the long TM1 and TM6 helices, is loosely packed against the core domain (Fig. 1, C and D). The core domain shares structural similarity with NCX_Mj (*10*); their N and C terminal halves (TM2 to TM5 and TM7 to TM10, respectively) are related by a pseudo twofold rotational axis within the molecule. The two conserved α-repeats (*6*) consist of TM2 and TM3 for α-1 and TM7 and TM8 for α-2 (figs. S5 and S6). CAX_Af contains two additional TM helices

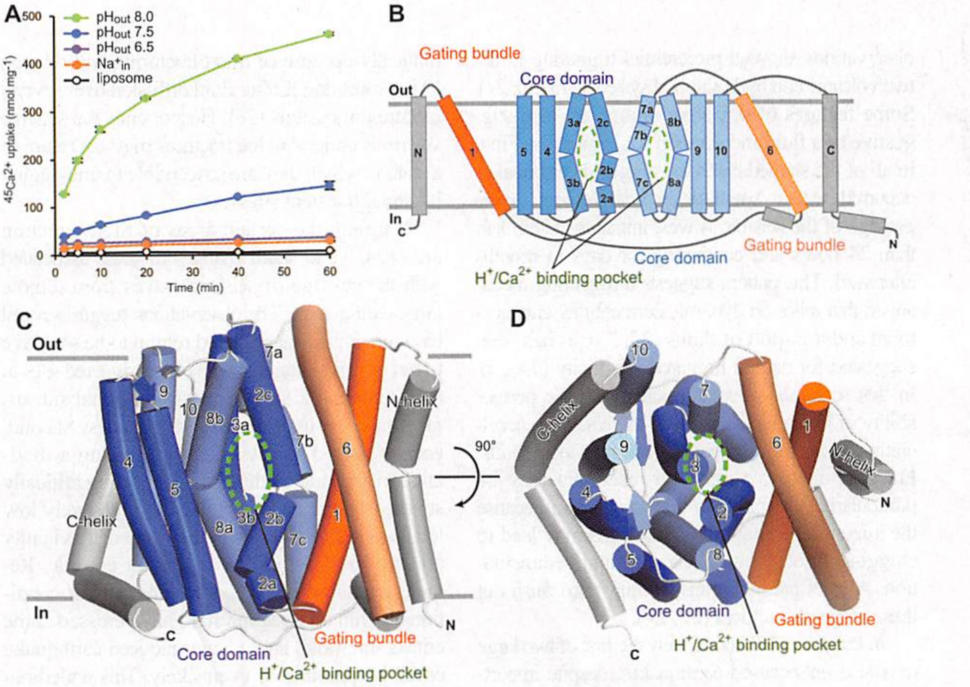

Fig. 1. The overall structure and function of CAX_Af. **(A)** Time courses of $^{45}Ca^{2+}$ uptake by liposome-reconstituted CAX_Af at different pH values. **(B)** Schematic representation of the CAX_Af topology. The core domain and the gating bundle are colored blue and orange, respectively. The additional helices are gray. The H^+/Ca^{2+} binding pockets are indicated by green dotted circles. **(C and D)** Structure of CAX_Af (mol A) as viewed from (C) the membrane plane or (D) the extracellular side. The color coding is the same as in (B).

---

[1] Department of Biophysics and Biochemistry, Graduate School of Science, University of Tokyo, 2-11-16 Yayoi, Bunkyo-ku, Tokyo 113-0032, Japan. [2] RIKEN Advanced Science Institute, 2-1 Hirosawa, Wako-shi, Saitama 351-0198, Japan. [3] Department of Pharmacology, Faculty of Medicine, Fukuoka University, 7-45-1 Nanakuma, Jonan-ku, Fukuoka 814-0180, Japan. [4] Department of Bioengineering Sciences, Graduate School of Bioagricultural Sciences, Furo-cho, Chikusa-ku, Nagoya 464-8601, Nagoya University, Japan. [5] RIKEN SPring-8 Center, Hyogo 679-5148, Japan. [6] Graduate School of Medicine and Faculty of Medicine, Kyoto University, Konoe-cho Yoshida Sakyo-ku Kyoto 606-8501, Japan.

*Corresponding author. E-mail: nureki@biochem.s.u-tokyo.ac.jp (O.N.); ishitani@biochem.s.u-tokyo.ac.jp (R.I.)